How to cite: *Angew. Chem. Int. Ed.* **2022,** *61,* e202208951
International Edition: doi.org/10.1002/anie.202208951
German Edition: doi.org/10.1002/ange.202208951

Protocells

Mechanistic Insights into the Phase Separation Behavior and Pathway-Directed Information Exchange in all-DNA Droplets

*Wei Liu, Avik Samanta, Jie Deng, Cecilia Oluwadunsin Akintayo, and Andreas Walther**

Abstract: Liquid-liquid phase separation provides a versatile approach to fabricating cell-mimicking coacervates. Recently, it was discovered that phase separation of single-stranded DNA (ssDNA) allows for forming protocells and microgels in multicomponent systems. However, the mechanism of the ssDNA phase separation is not comprehensively understood. Here, we present mechanistic insights into the metal-dependent phase separation of ssDNA and leverage this understanding for a straightforward formation of all-DNA droplets. Two phase separation temperatures are found that correspond to the formation of primary nuclei and a growth process. Ca^{2+} allows for *irreversible*, whereas Mg^{2+} leads to *reversible* phase separation. Capitalizing on these differences makes it possible to control the information transfer of one-component DNA droplets and two-component core–shell protocells. This study introduces new kinetic traps of phase separating ssDNA that lead to new phenomena in cell-mimicking systems.

Introduction

In living cells, liquid-liquid phase separation (LLPS) has been identified as a fundamental phenomenon that drives the assembly of various biomacromolecules into dynamic, often liquid-like colloidal entities.[1] The generation of these biological condensates involves for instance demixing of specific proteins with recognition domains and RNAs in a pathway commonly known as complex coacervation.[2] Some of the well-known cellular membrane-less organelles include nucleoli,[3] Cajal bodies[4] and promyelocytic leukemia nuclear bodies in the nucleus,[5] while germ granules and stress granules form in the cytoplasm.[6] As the evidence of numerous subcellular functions and biochemical pathways presenting in these condensates—such as signal transduction, RNA metabolism, DNA damage response, and ribosomal biogenesis—are mounting,[7] an interest in employing similar LLPS-driven compartments as an *ex vivo* protocellular model[8] has been rising in the urge of designing soft materials with life-like traits.

In contrast to oil droplets, coacervates formed via different pathways,[9] such as phase separation of solutes utilizing homolytic interactions or complex coacervation by heterotypic interactions of oppositely charged solutes, contain a large amount of water providing a hydrodynamic molecularly crowded confinement in which enzymes,[10] and ribozymes[11] can be active. In recent years, complex coacervates have been recognized as a more suitable protocell model with respect to classical liposomes,[12] polymersomes,[13] colloidosomes,[14] proteinosomes,[15] due to their molecularly crowded interior resembling the cytoplasmic confinement as well as their ability to ensure facile exchange of matter/energy with their surroundings without employing complex transport machinery. Even though complex coacervates using biologically relevant synthetic constituents, such as short oligonucleotide[1c,10d,16] and peptides,[8a,17] have been reported, achieving control over morphology and dynamic behavior of droplets by varying the biological information encoded in the constituents, such as nucleotide sequence, remains challenging.

Since DNA has emerged as a powerful building block for developing hierarchical nano/microstructures because of its programmability and sequence-specificity, engineering all-DNA coacervates in a bottom-up approach would provide a platform to study chemical reactions and self-assembly processes in a DNA-based crowded environment. There have been reports on designing DNA-rich microgels using multivalent cross-linking of X- and Y-tiles,[18] whereas we have recently reported the formation of all-DNA coacervates by simple phase separation of polyadenine (polyA)-rich ssDNA polymers.[10c,19] This approach provides ample parameters (e.g., temperature, ionic strength, DNA chain length) to modulate the morphological and physical

[*] W. Liu, Dr. A. Samanta, Dr. J. Deng, C. O. Akintayo, Prof. Dr. A. Walther
Life-Like Materials and Systems, Department of Chemistry, University of Mainz
Duesbergweg 10–14, 55128 Mainz (Germany)
E-mail: andreas.walther@uni-mainz.de
C. O. Akintayo, Prof. Dr. A. Walther
Cluster of Excellence livMatS @ FIT—Freiburg Center for Interactive Materials and Bioinspired Technologies, University of Freiburg
Georges-Köhler-Allee 105, 79110 Freiburg (Germany)
Dr. J. Deng
Present address: Department of Cancer Biology, Dana-Farber Cancer Institute and Wyss Institute for Biologically Inspired Engineering, Harvard Medical School
Boston, MA 02115 (USA)

properties of the resulting coacervates. We showed that a plethora of all-DNA mesoscopic structures could be realized by combining the phase separation behavior with canonical DNA duplex recognition, leading to capsules or core–shell structures. Although complex structures could be reliable formed by kinetic pathway guidance during temperature ramps, details of the structure formation pathways and a quantitative understanding remain elusive.

In this article, we report a detailed mechanistic understanding of the DNA demixing behavior, and illustrate two different metal ion-dependent phase separation pathways (Ca^{2+} vs. Mg^{2+}). We demonstrate that the phase separation process is in fact a two-stage process and that this heat-induced LLPS is only *reversible* for Mg^{2+}, but all-DNA coacervate droplets remain stable after cooling for Ca^{2+}. This new Ca^{2+}-specific kinetic trapping can be utilized for simple Ca^{2+}/all-DNA droplet formation, and also opens a new design space to trigger information exchange between coacervates and protocells stemming from distinct ion-specific pathways.

Results and Discussion

Previously, we demonstrated that adenine (A) and thymine (T)-rich ssDNA polymers (namely $p(A_{20}\text{-i})_x$ and $p(T_{20}\text{-j})_y$) exhibit different phase separation behavior in the presence of divalent counterions.[19a] The repeating units of the ssDNA consist of a A_{20} block (or T_{20} block) and a 21 nucleobases (nb) long barcode sequence i (or j). The barcode sequences are used to post-functionalize the droplets with dye-appended complementary strands (e.g., dye-conjugated i* or j* for visualization), and have been chosen to avoid self-dimerization and hairpin formation. Additionally, the i/i* and j/j* ($T_m \approx 65\,°C$) duplexes are stable at room temperature (RT). Our previous focus had been on Mg^{2+}—the most commonly used bivalent counterion for DNA nanoscience—for which we could show that $p(A_{20}\text{-i})_x$ features a length- and Mg^{2+}-concentration-dependent lower critical solution temperature (LCST) behavior and undergoes a *reversible* heat-driven solubility-to-insolubility transition. On the contrary, $p(T_{20}\text{-j})_y$ remains in solution at similar Mg^{2+} concentration when heated. We also reported that this sequence-dependent LCST behavior can be leveraged for pathway-dependent core–shell like $p(A_{20}\text{-i})_x$/$p(T_{20}\text{-j})_y$ protocell formation using a simple temperature ramp, during which the polyA-rich demixed phase is kinetically trapped during cooling by hybridization with polyT-rich ssDNA.

In contrast to earlier work on Mg^{2+} ions, we herein focus largely on Ca^{2+} ions for which we identify subtle but important differences, in particular with respect to the reversibility and sequence-specificity of the phase separation processes. In more detail, we present a more straightforward pathway to form independent all-DNA $p(A_{20}\text{-i})_x$ and $p(T_{20}\text{-j})_y$ droplets—stable at RT—using an *irreversible* heat-triggered phase separation process in the presence of Ca^{2+} ions (Figure 1a–c). We also demonstrate that the phase separation of $p(A_{20}\text{-i})_x/Ca^{2+}$ passes through two different

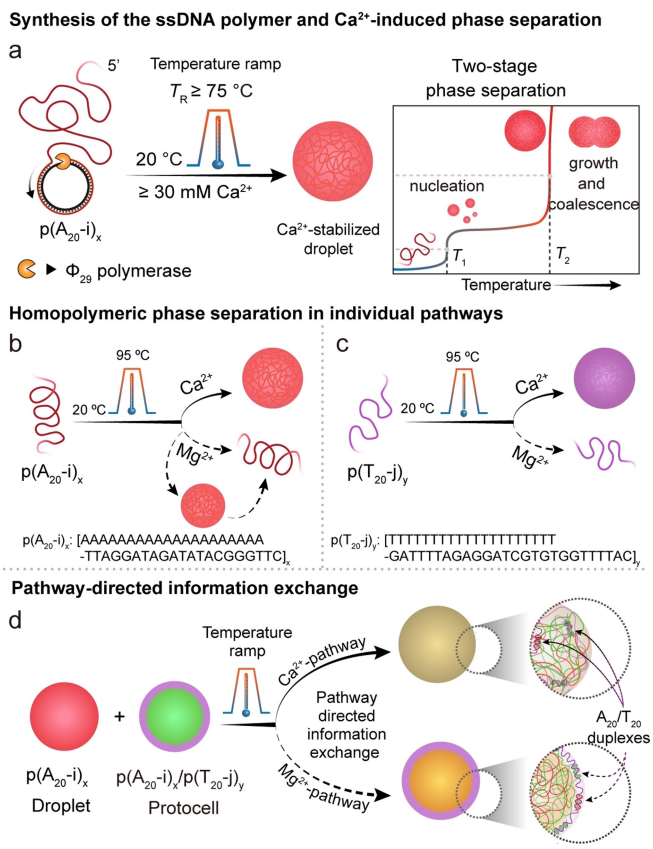

Figure 1. Schematic illustration of the synthesis, metal-dependent phase separation, and information exchange of all-DNA droplets. a) Synthesis of all-DNA multiblock copolymers via rolling circle amplification (RCA), and two-stage droplet formation process. b) Phase separation of $p(A_{20}\text{-i})_x$ with Ca^{2+} and Mg^{2+} ions via a temperature ramp. $p(A_{20}\text{-i})_x$ undergoes *irreversible* phase separation with Ca^{2+} and *reversible* phase separation with Mg^{2+}. c) Phase separation of $p(T_{20}\text{-j})_y$ occurs only in the presence of Ca^{2+} and not for Mg^{2+}. d) Pathway controlled information exchange by mingling interactions of droplet and protocell mixtures by Ca^{2+}-pathway and Mg^{2+}-pathway.

transition temperatures during the heating, confirming a nucleation and growth mechanism for the formation of $p(A_{20}\text{-i})_x$ droplets (Figure 1a). In more detail, we report a detailed mechanistic study to explain the Ca^{2+}-dependent coacervation pathway by varying the ssDNA chain length, Ca^{2+} concentration, and incubation temperature using real-time monitoring of the cloud point behavior and morphological development by *in situ* confocal laser scanning microscopy (CLSM) and dynamic light scattering (DLS). Whenever needed we also compare to the Mg^{2+}-dependent pathway. Furthermore, we capitalize on the understanding of the differences between *reversible* Mg^{2+}-type phase separation and *irreversible* Ca^{2+}-type phase separation to establish coacervate-protocell communication and information exchange by mingling the interactions inherent to the Ca^{2+} and Mg^{2+}-coacervation pathways (Figure 1d).

Firstly, to understand the effect of the ssDNA chain length on the phase separation behavior, we synthesized two ssDNA polymers ($p(A_{20}\text{-i})_x$ and $p(T_{20}\text{-j})_y$) using an isothermal enzymatic polymerization technique, namely RCA.[20]

This method yields extremely long sequence-specific multiblock copolymers that are complementary to the sequence encoded in a circular DNA template. Notably, shorter ssDNA multiblock copolymers with varying repeat lengths, x, can be obtained using heat-induced cleavage[19a] of the RCA product at different incubation times. In total, we prepared six $p(A_{20}\text{-i})_x$ polymers with $x \approx 12$–56 by heating to 95 °C for 5 to 90 min. The average x was calculated from agarose gel electrophoresis (AGE) in Figure 2a–c.

Temperature-dependent turbidity measurements at 350 nm (away from the intrinsic DNA absorbance at 260 nm) and DLS allow to analyze the phase separation behavior of $p(A_{20}\text{-i})_x$ with various chain lengths, and at different Ca^{2+} concentrations (Figure 2d,e). We first focus on the effect of chain length. Interestingly, two transition temperatures (T_1 and T_2) are visible while heating the same ssDNA mass concentration of $p(A_{20}\text{-i})_x/Ca^{2+}$ mixture from 20 °C to 80 °C at 1 °C min^{-1} (Figure 2d). Upon increase of the $p(A_{20}\text{-i})_x$ length from $x = 12$ to 56, T_1 decreases slightly from 40.2 °C to 37.1 °C, and T_2 increases slightly from 75.4 °C to 76.5 °C. The decrease of T_1 with increasing x is in line with general polymer demixing. We suggest—and later provide more evidence—that T_1 and T_2 indicate the nucleation and the growth processes of the phase separation pathway,

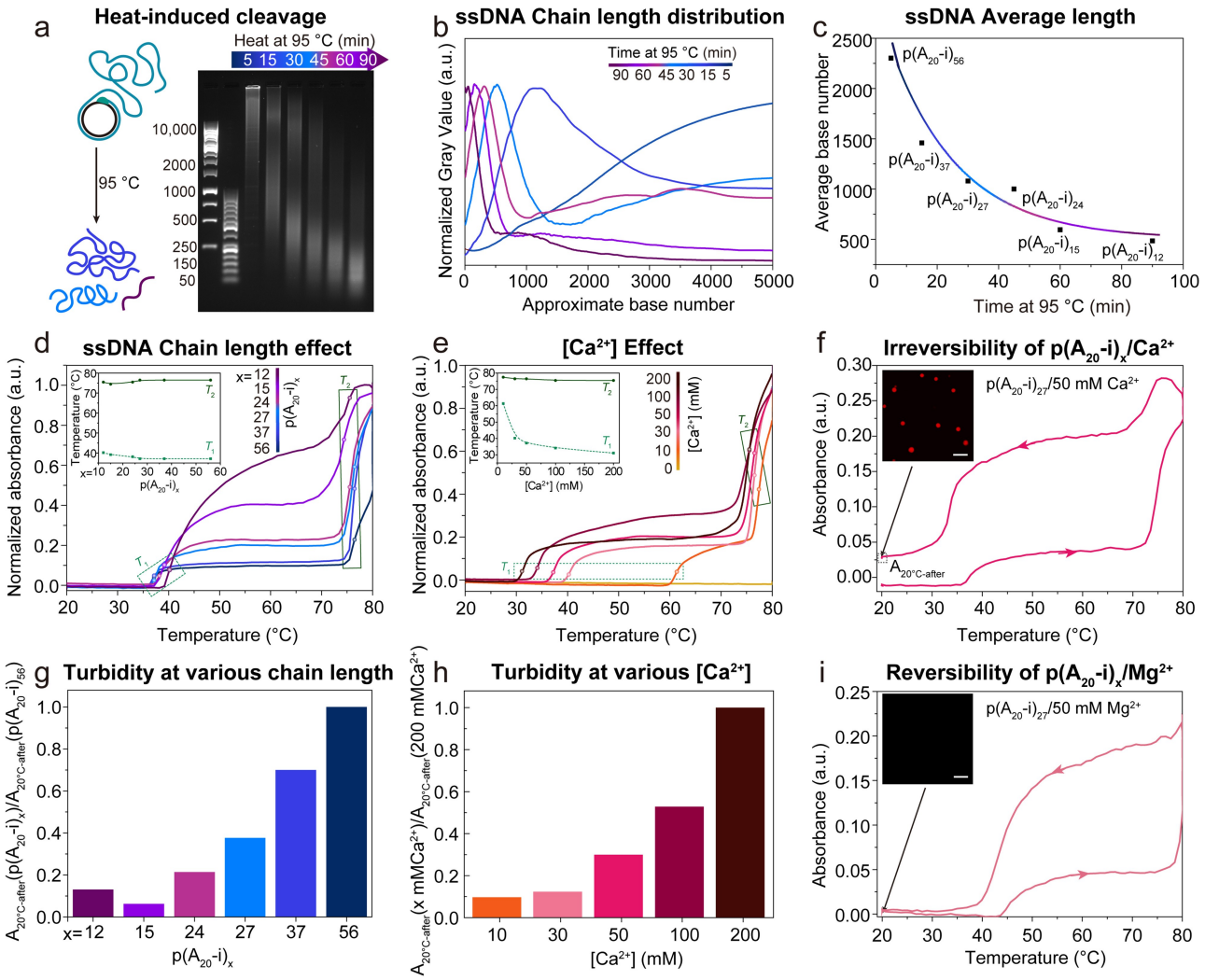

Figure 2. Effect of ssDNA chain length and Ca^{2+} concentration on thermo-responsive phase separation. a) Time-dependent AGE for the thermal cleavage of $p(A_{20}\text{-i})_x$ by heating to 95 °C for different incubation times (5, 15, 30, 45, 60, 90 min). b) Corresponding greyscale analysis of AGE with $p(A_{20}\text{-i})_x$ length as calculated from the DNA ladders (50 bp and 1k bp). c) Average length of $p(A_{20}\text{-i})_x$ with incubation time. The actual chain length at short times is longer than this calculated average length because some long DNA strands, especially those longer than 10k (the upper limit of the ladder), cannot be counted. d) Temperature-dependent absorbance at 350 nm of $p(A_{20}\text{-i})_x$/50 mM Ca^{2+} with different chain lengths. The inset shows T_1 and T_2 with different chain lengths. e) Temperature-dependent absorbance at 350 nm of $p(A_{20}\text{-i})_{27}/Ca^{2+}$ at varying Ca^{2+} concentrations. The inset shows T_1 and T_2 with different Ca^{2+} concentrations. f) Cyclic temperature ramp showing absorbance at 350 nm of $p(A_{20}\text{-i})_{27}$/50 mM Ca^{2+}. The inset displays a CLSM image after the heating/cooling cycle. g) Turbidity of $p(A_{20}\text{-i})_x$/50 mM Ca^{2+} with different chain lengths at 20 °C after heating/cooling cycle. h) Turbidity of $p(A_{20}\text{-i})_{27}/Ca^{2+}$ with varying Ca^{2+} concentrations at 20 °C after heating/cooling cycle. i) Cyclic temperature ramp showing absorbance at 350 nm of $p(A_{20}\text{-i})_{27}$/50 mM Mg^{2+}. The inset displays a CLSM image after the heating/cooling cycle. Temperature ramp rate: 1 °C min^{-1}. Scale bar: 10 μm.

respectively. The ssDNA polymers $p(A_{20}\text{-}i)_x$ nucleate into small stable nanoscopic seeds above T_1, and as the temperature reaches T_2, the seeds quickly grow and coalesce, leading to the formation of microscopic droplets. Additionally, a plateau in the scattering intensities between T_1 and T_2 appears for $p(A_{20}\text{-}i)_x$ with $x > 15$. This observation indicates that the $p(A_{20}\text{-}i)_x$ with $x \leq 15$ shorter chain length exhibits a more gradual growth, while the longer $p(A_{20}\text{-}i)_x$ experiences a sudden aggregation at T_2. We selected $p(A_{20}\text{-}i)_{27}$ to investigate the effect of the Ca^{2+} concentration on the phase separation (Figure 2e). In absence of Ca^{2+}, $p(A_{20}\text{-}i)_{27}$ does not show phase separation. However, two transition temperatures appear consistently for higher Ca^{2+} concentrations. The influence of the Ca^{2+} concentration is much more profound on the details of the phase separation as compared to the influence of chain length. The T_1 decreases strongly from 61.4 °C to 31.1 °C when increasing the Ca^{2+} concentration from 10 mM to 200 mM, whereas T_2 exhibits a slight decrease from 77.5 °C to 75.5 °C. This indicates that varying the Ca^{2+} concentration dramatically alters the primary nucleation temperature (T_1) even though the growth temperature (T_2) is not largely affected.

Since a detailed understanding of the phase separation behavior is crucial for constructing complex mesoscopic all-DNA droplet morphologies, we paid acute attention to potential differences between the previously established Mg^{2+}-type phase separation[10c,19a] and the Ca^{2+}-dependent pathway discovered here. The most critical and consistent observation is the *reversibility* of the phase separation in the case of Mg^{2+}, whereas the phase separation is *irreversible* for Ca^{2+} as highlighted in the heating/cooling cycles in Figure 2f,i. The behavior is robust and can be repeated as shown in Figure S2a,b. Substantial scattering remains after cooling of $p(A_{20}\text{-}i)_{27}/Ca^{2+}$ (Figure 2f), whereas the turbidity completely disappears for $p(A_{20}\text{-}i)_{27}/Mg^{2+}$. Correspondingly, CLSM after cooling does not show any structures for the Mg^{2+}-based system, whereas plenty of DNA droplets with ≈ 2 μm diameter are observed for the Ca^{2+}-pathway (Figure 2f,i; inset). Notably, the decrease in turbidity from high temperature to RT in the $p(A_{20}\text{-}i)_{27}/Ca^{2+}$ system does not need to arise from a partial re-dissolution, but rather stems from a reswelling of the collapsed droplets which goes along with a lower refractive index mismatch between the coacervate and the solution that causes the scattering. The resulting droplets are stable at RT for weeks. The remaining turbidity is a function of the chain length and the Ca^{2+} concentration, which reflects size (see also below, Figure 4c,d) and compaction, respectively (Figure 2g,h). The Ca^{2+} concentration is expected to lead to different swelling after the heating/cooling cycle, which again rather influences the refractive index contrast and not the particle fraction. Critically, these observations reveal a new Ca^{2+}-induced pathway for forming stable all-DNA droplets without any auxiliary agents to arrest the metastable coacervates kinetically. Previously a surface complexing $p(T_{20}\text{-}j)_y$ or a palindromic, self-crosslinking XL domain in $p(A_{20}\text{-}i\text{-}XL)_x$ was needed in the Mg^{2+}-pathway to stabilize any reversibly forming polyA droplets at high temperature.[19a]

To better understand this new Ca^{2+}-pathway for all-DNA droplet formation, we investigated structure formation via CLSM in both *ex situ* and *in situ* experimental setups (Figure 3a,f,h,j). For the *ex situ* measurements, we heated and incubated (5 min) a mixture of $p(A_{20}\text{-}i)_{27}$ and 50 mM Ca^{2+} at different top temperatures during a temperature ramp. After the cooling step, a stoichiometric amount of a complementary dye-labeled ssDNA ($Atto_{647}$-i*) was added for CLSM as $Atto_{647}$-i* binds to the barcode i. A series of CLSM micrographs (Figure 3b and Figure S1a,b) shows that distinct spherical droplets can be observed only when the incubation temperature of the temperature ramp reaches 75 °C. No droplets are formed below 75 °C. This ramp temperature is close to the T_2 (76.5 °C) of $p(A_{20}\text{-}i)_{27}$ in the Ca^{2+}-pathway (Figure 2e) and indeed confirms that larger scale aggregation by growth and coalescence can only be observed when heating to or above T_2. The droplet size increases when the incubation temperature is elevated from 75 °C to 95 °C, as derived from statistical image analysis (Figure 3d,e). To understand structural processes in the turbidity plateau region between T_1 and T_2, we conducted DLS at RT and at 55 °C (Figure 3c). An evident change in size occurs from a population of dissolved ssDNA polymers with a $< D_h >_z$ of ca. 20 nm at RT to a $< D_h >_z$ of ca. 200 nm at 55 °C. The DLS count rate also increases from 3.9 to 34.9 $kHz\,mW^{-1}$ (Figure 3c), which aligns with the turbidity increase seen in UV-Vis temperature ramps (Figure 2d–f). Obviously, such structures are below the resolution limit of the CLSM. Since the equilibration process in the DLS is slow compared to the temperature ramp used in a thermocycler, a stable collapse and the formation of primary nuclei at this temperature can be concluded. Hence, these observations support the phase separation pathway determined from the UV-Vis spectroscopy, with a primary nucleation step above T_1 and rapid microdroplet formation by growth and coalescence at T_2.

For visual observation of the droplet formation process, we also performed *in situ* CLSM imaging using a heating stage to monitor the structural transformations during a heating cycle (25→85 °C) of a mixture of $p(A_{20}\text{-}i)_{27}$ in the presence of 50 mM Ca^{2+}. For this purpose, we synthesized a covalently labeled $p(A_{20}\text{-}i)_{27}$-Cy5 by co-polymerizing a dUTP–Cy5 monomer (≈ 2 % of dTTP) during the RCA process, which makes the ssDNA polymer intrinsically fluorescent. No distinguishable structures are observed until the temperature reaches ≈85 °C. A population of droplets appears after 20 s at 85 °C, and successively, the spherical droplets grow in size and eventually undergo coalescence (Figure 3g,i). The coalescence of the droplets at 85 °C indicates a dynamic behavior of the phase-separated droplets (Figure 3i). We also heated the sample only to the plateau between T_1 and T_2. Similar to the DLS results, CLSM does not show any structures, even using a much slower heating rate and maintaining the temperature for ca. 5 min (Figure 3j,k). These *in situ* CLSM imaging results, together with the DLS data, confirm the presence of a nucleation step with stable nuclei above T_1 and a subsequent growth and coalescence phase above T_2, which is termed as a "two-stage process" .

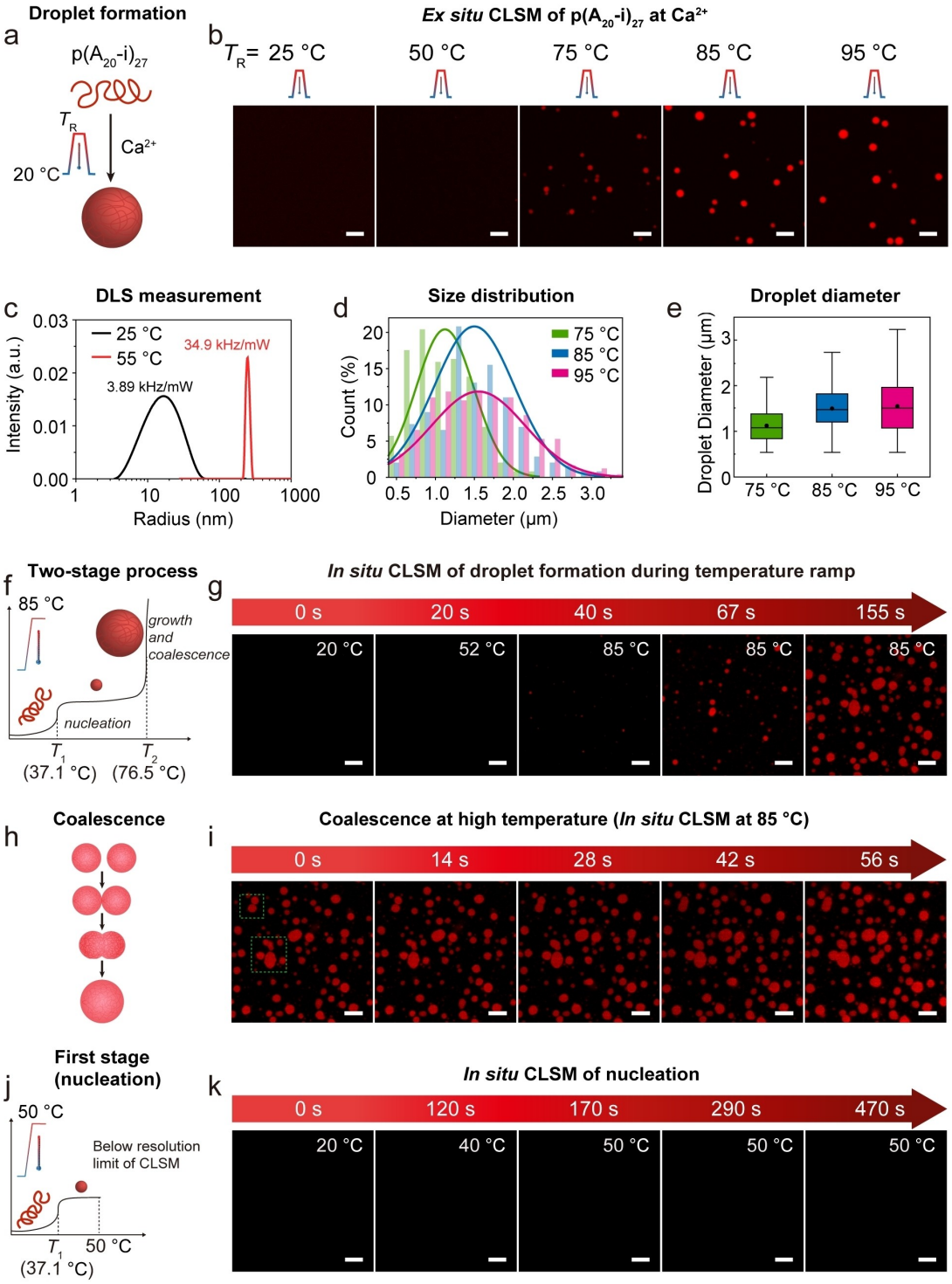

Figure 3. Formation of polyA DNA droplets via the Ca^{2+}-pathway. a) Schematic illustration of the formation of droplets. b) *Ex situ* CLSM images of 0.08 g L^{-1} solution of $p(A_{20}\text{-}i)_{27}$ with 50 mM Ca^{2+} after incubating at different temperatures for 5 min with a heating and cooling rate of 3 °C s^{-1}. Imaging is done after the completion of the temperature ramp. A minimum temperature of 75 °C is needed for visible droplet formation. c) Diameter profile of 0.003 g L^{-1} solutions of $p(A_{20}\text{-}i)_{27}$ with 50 mM Ca^{2+} measured by DLS at RT and 55 °C. d) Diameter distribution from (b). e) Droplet diameter from (b). The point and line inside the box correspond to the mean and median line of the droplet population. The box represents a five-number summary of the droplet data set, extending from the first quartile to the third quartile. Error bars are the standard deviation of ca. 30 droplet counts. f) Two-stage phase separation of $p(A_{20}\text{-}i)_{27}$ via the Ca^{2+}-pathway. g) *In situ* CLSM images of 0.12 g L^{-1} solution of $p(A_{20}\text{-}i)_{27}$-Cy5 with 50 mM Ca^{2+} during heating to 85 °C and maintaining at 85 °C with a heating rate of 1.5 °C s^{-1}. h) Schematic illustration of the coalescence of DNA droplets. i) *In situ* CLSM images of the coalescence of droplets at 85 °C. j) The first stage of phase separation (nucleation) of $p(A_{20}\text{-}i)_{27}/Ca^{2+}$. (k) *In situ* CLSM images of 0.12 g L^{-1} solution of $p(A_{20}\text{-}i)_{27}$-Cy5 with 50 mM Ca^{2+} during heating to 50 °C with a heating rate of 0.15 °C s^{-1}. Scale bar: 5 µm.

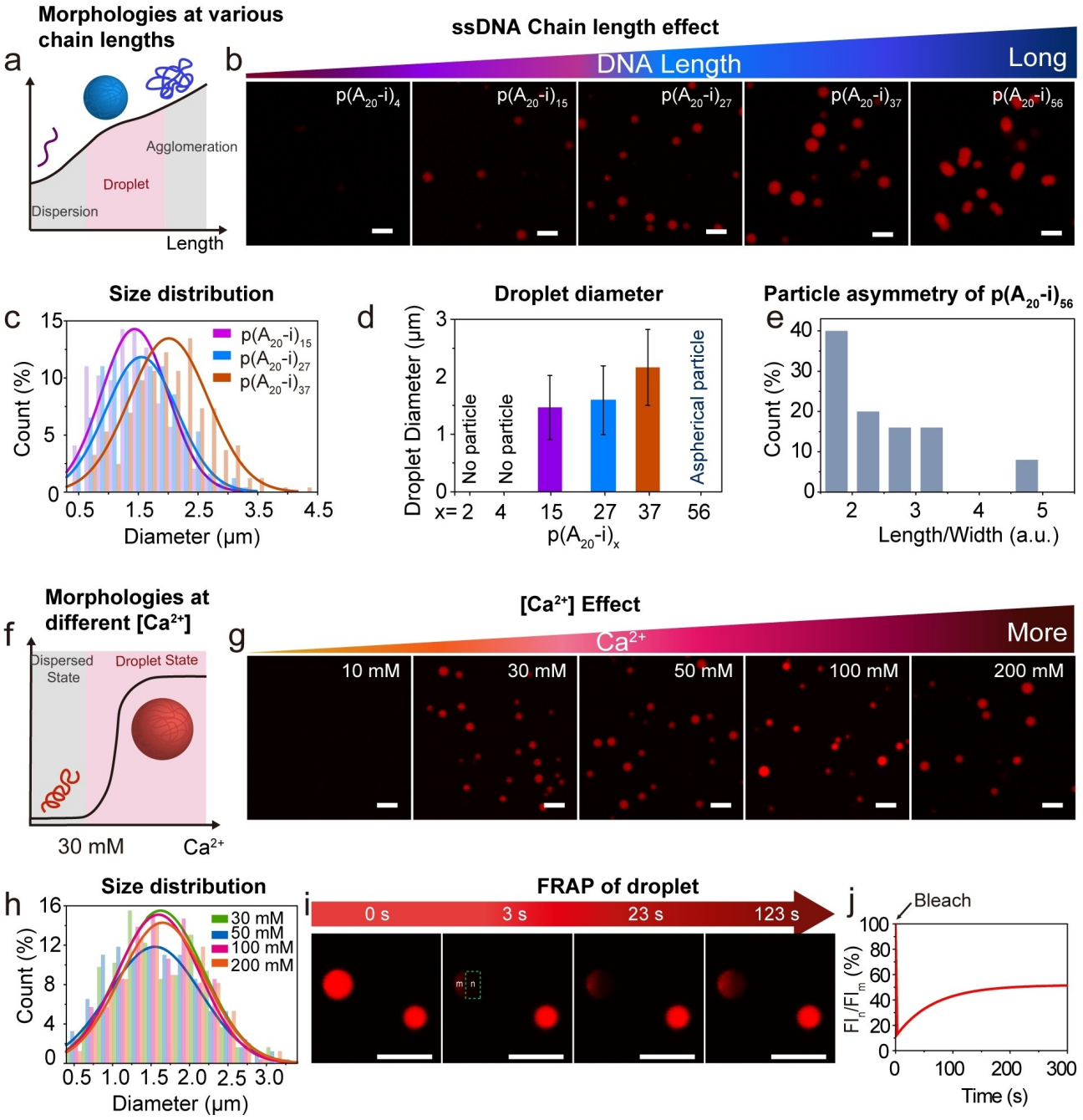

Figure 4. Effect of polyA chain length and Ca^{2+} concentration on droplet formation and properties. a–e) Effect of ssDNA chain length. a) Schematic illustration of $p(A_{20}\text{-}i)_x/Ca^{2+}$ morphologies with different chain lengths. b) CLSM images of 0.08 g L^{-1} solution of $p(A_{20}\text{-}i)_x$/50 mM Ca^{2+} with an increasing chain length. c) Size distribution of droplet from (b). d) Droplet diameter distribution. Error bars correspond to standard deviations from three duplicate experiments. Ca. 300 droplets were counted. e) Particle asymmetry of $p(A_{20}\text{-}i)_{56}/Ca^{2+}$ from (b). f–h) Effect of Ca^{2+} concentration. f) Schematic illustration of $p(A_{20}\text{-}i)_{27}/Ca^{2+}$ morphologies at different Ca^{2+} concentrations. g) CLSM images of 0.08 g L^{-1} solution of $p(A_{20}\text{-}i)_{27}/Ca^{2+}$ with an increasing Ca^{2+} concentration. h) Size distribution of droplets from (g). i–j) FRAP of $p(A_{20}\text{-}i)_{27}$/50 mM Ca^{2+} droplet. i) CLSM images of the droplets during a FRAP experiment: pre-bleach (0 s), bleach (3 s), after-bleaching (23 s and 123 s). j) The corresponding fluorescence intensity from (i) confirms the $p(A_{20}\text{-}i)_x/Ca^{2+}$ droplet to have a rather gelled interior. The temperature ramp to 95 °C for 5 min at a heating and cooling rate of 3 °C $s^{-1}$is used for all the experiments unless otherwise specified. Scale bar: 5 μm.

For a more comprehensive understanding, we also investigated whether this two-stage process also holds for the phase separation of $p(A_{20}\text{-}i)_{27}$ with 50 mM Mg^{2+}. Indeed, Figure S3 also shows the absence of any structures by CLSM in the plateau between T_1 and T_2, thus also confirming a nucleation and growth process. Hence, despite mechanistic similarities between Ca^{2+} and Mg^{2+} in the two-stage process during phase separation, the reversibility of the process is fundamentally different, which relates to the binding interaction of polyA chains with both ions. Previous reports have

indicated a higher binding affinity of Ca^{2+} over Mg^{2+} with DNA oligomers in solution,[21] and this difference is accentuated at a high concentration of DNA.[21b,22] The higher binding affinity of Ca^{2+} to polyA and polyT chains can be attributed to its more polarizable aqueous shell,[23] enhancing the interaction with the nucleobases apart from the phosphate backbone.[24] Thus, we hypothesize that the higher interaction of the DNA polymers with Ca^{2+} and low chain mobility in the coacervate state causes permanent kinetic trapping of the droplets.

Furthermore, we investigated the effect of the ssDNA chain length and the Ca^{2+} concentration on the droplet morphology using CLSM at a constant top temperature in the temperature ramp of 95 °C. Figure 4a–e and Figure S1c–e show that spherical droplets with moderate dispersity can be formed for $p(A_{20}\text{-}i)_x$ with x between 15 to 37 (50 mM Ca^{2+}). Longer chain lengths, such as $p(A_{20}\text{-}i)_{56}$, lead to aspherical morphologies that arise from coalescence and insufficient mobility of long chains to regain a spherical droplet state.[25] Very short chain lengths ($x < 15$) do not lead to specific structures, which we relate to insufficient kinetic trapping of the phase-separated state (Figure 4b). Hence, to synthesize spherical all-DNA droplets via Ca^{2+}-pathway, the optimum number of repeating units in $p(A_{20}\text{-}i)_x$ lies in the range of ≈15–37 (Figure 4d) to balance phase separation propensity and chain dynamics that are both a function of the polymer length. As for the influence of Ca^{2+}, we prepared several $p(A_{20}\text{-}i)_{27}$ mixtures with varying Ca^{2+} concentrations from 0 to 200 mM. Figure 4f–h and Figure S1f,g depict spherical droplets with moderate dispersity for $Ca^{2+} \geq 30$ mM, setting the lower limit for efficient kinetic trapping of the high temperature-induced morphology.

As mentioned above, the $p(A_{20}\text{-}i)_x$ droplets formed via the Mg^{2+}- pathway at elevated temperature dissolve at RT, while the droplets formed via the Ca^{2+}-pathway remain stable at RT. Hence, it is of particular interest to understand the physical state of the droplet interior stabilized at RT formed via the Ca^{2+}-pathway, which is elucidated by fluorescence recovery after photobleaching (FRAP; Figure 4i,j). Approximately 40 % of the fluorescence is recovered after 5 min when a part of a droplet is bleached using a 638 nm laser line, indicating a slow diffusion of the polymer chains in the coacervate state, and a rather gelled interior. Our previous work demonstrated that the fluorescence of $p(A_{20}\text{-}i)_x/p(T_{20}\text{-}j)_y$ protocells with liquid polyA cores formed with Mg^{2+} can be fully recovered in a few seconds.[19a] This indicates that these Ca^{2+}-based $p(A_{20}\text{-}i)_{27}$ droplets are more solid than the Mg^{2+}-based $p(A_{20}\text{-}i)_{27}/p(T_{20}\text{-}j)_{27}$ protocells, underscoring a difference in binding of Ca^{2+} vs. Mg^{2+} with the polyA chains.

After having understood mechanistic details on the Ca^{2+}-mediated phase separation of $p(A_{20}\text{-}i)_x$ and its important difference to the Mg^{2+}-mediated phase separation, we raised the question to what extent more complex morphologies can be built up, and whether this new type of kinetic trap can be leveraged for new structure formation pathways. For instance, previously, we could show that a temperature ramp of reversibly phase-separating $p(A_{20}\text{-}i)_x$ in presence of permanently soluble $p(T_{20}\text{-}j)_y$ allows for the formation of core–shell DNA protocells in the presence of Mg^{2+} ions.[19a] This process is shown in Figure 5c,d. The important prerequisite for this process to work is the solubility of $p(T_{20}\text{-}j)_y$ across the full temperature ramp. However, when $p(T_{20}\text{-}j)_{27}$ is subjected to a temperature ramp at 50 mM Ca^{2+} also $p(T_{20}\text{-}j)_{27}$ coacervates are found (Figure 5b). This underscores—similar to $p(A_{20}\text{-}i)_x$—that Ca^{2+} leads to a stronger propensity for phase separation and to a lower nucleobase specificity (Figure 5a,b and Figure S4a,b). Interestingly, when subjecting a mixture of $p(A_{20}\text{-}i)_{27}$ and $p(T_{20}\text{-}j)_{27}$ to a temperature ramp in the presence of 50 mM Ca^{2+}, an Mg^{2+}-induced protocell architecture cannot be found; instead, mixed coacervates containing both ssDNA equally distributed within the droplet are found (Figure 5c). In addition to phase separation by Ca^{2+}, the mixed DNA domains are now additionally stabilized via $A_{20}\text{-}T_{20}$ duplex formation during cooling.

On a system level, we hypothesized that such salt-dependent morphologies could be used to create new coacervate structures by mixing multiple coacervate systems and exposing them to a second temperature ramp. To this end, we mixed Ca^{2+}-based $p(A_{20}\text{-}i)_{27}$ droplets (red in Figure 5f) with Mg^{2+}-based $p(A_{20}\text{-}i)_{27}/p(T_{20}\text{-}j)_{27}$ protocells (green and magenta, core and shell, Figure 5f) and investigated to what extent they can merge their "genetic content" embedded in the ssDNA sequence (Figure 5d,e). Prior to this, we first exchanged the buffer for 10 mM NaCl TE buffer, which led to a swelling of both entities, but complete dissolution was prevented in the protocells due to $A_{20}\text{-}T_{20}$ duplexes at the interface and in the Ca^{2+}-based $p(A_{20}\text{-}i)_{27}$ droplets due to some remaining Ca^{2+} (Figure 5g). After that, we again added new metal ions, Ca^{2+} or Mg^{2+}, to a total concentration of 50 mM.

When the resulting droplet/protocell mixture is subjected to a second temperature ramp, two different morphologies emerge via two different metal ion-dependent pathways (Figure 5e,f,h,k, Figure S5). In the Ca^{2+}-pathway, the droplets and protocells (both core and shell) undergo mixing with the formation of partly phase-separated Janus-type structures as well as mixed droplets (Figure 5h–j and Figure S5d). The initial protocells disappear and transform into homogeneously mixed coacervates due to the insolubility of the $p(T_{20}\text{-}j)_{27}$ in the presence of Ca^{2+} at elevated temperature. The line segment analysis on the final mixed droplets shows near homogeneous droplets (Figure 5i), and the observed Janus-like structures further confirm the coalescence behavior during the formation of the final mixed droplets (Figure 5j).

On the other hand, in the Mg^{2+}-dependent pathway, a core–shell protocell with mixed core emerges (Figure 5e,k). The $p(A_{20}\text{-}i)_{27}$ chains from both the droplet and the protocell integrate to form mixed protocell core. This is clearly seen in the superposition of the red fluorescence originating from the covalently labeled $p(A_{20}\text{-}i)_{27}$-Cy5 from the original Ca^{2+}-mediated droplet and of the green fluorescence emerging from the post-staining of $p(A_{20}\text{-}i)_{27}$, present in the Mg^{2+}-mediated protocell, with $Atto_{565}$-i*. Additionally, a clear shell of $p(T_{20}\text{-}j)_{27}$ post-stained with a magenta $Atto_{488}$-j* conjugate is visible. This homogeneous mixing in the core of

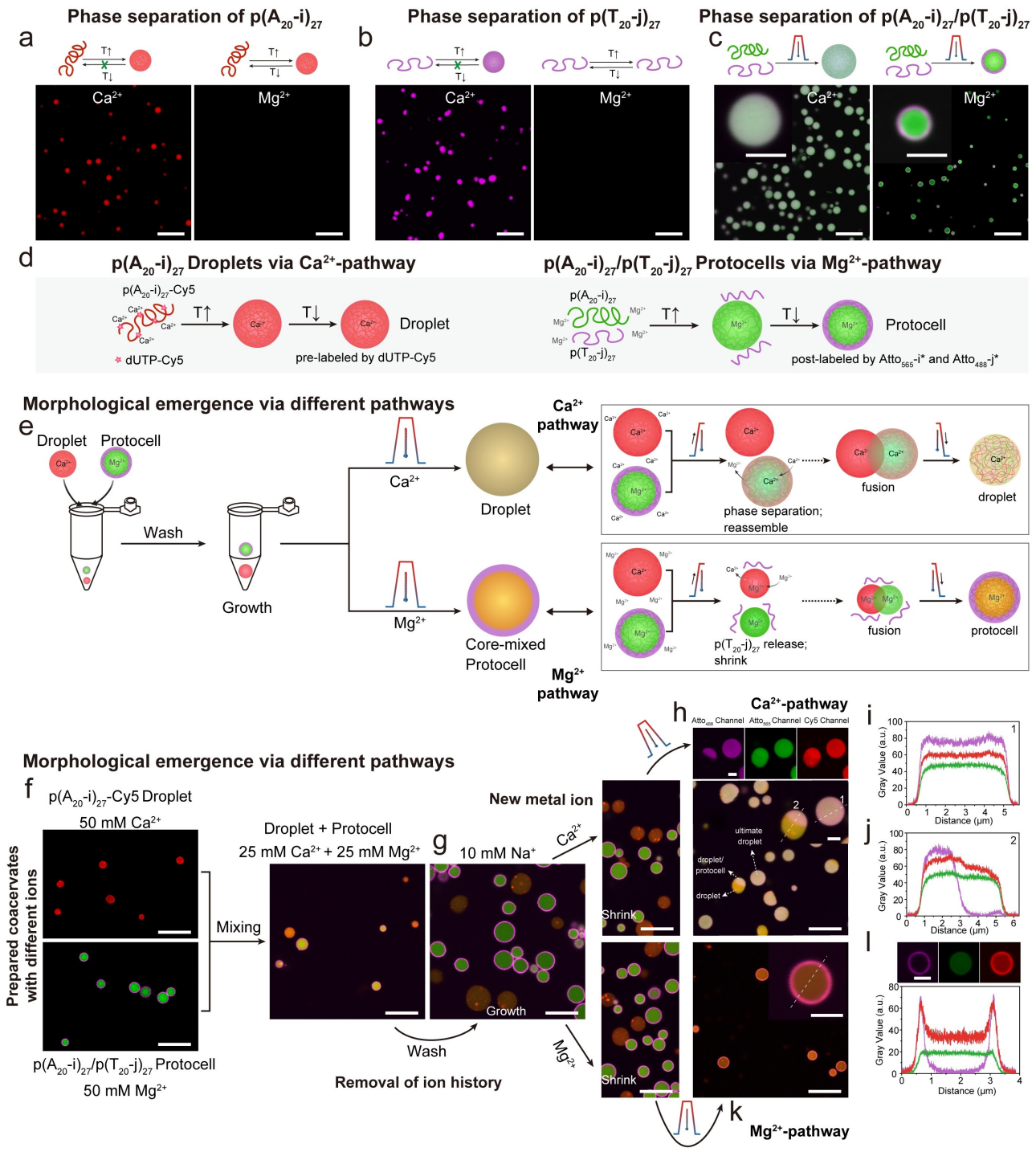

Figure 5. Information exchange between coacervate droplets and core–shell protocells in the presence of Ca^{2+} and Mg^{2+} ions. a) Reversibility of metal-dependent phase separation of $p(A_{20}\text{-}i)_{27}$. b) Reversibility of metal-dependent phase separation of $p(T_{20}\text{-}j)_{27}$. c) Complex morphologies can be obtained by subjecting a mixture of $p(A_{20}\text{-}i)_{27}$ and $p(T_{20}\text{-}j)_{27}$ to a temperature ramp at Ca^{2+} or Mg^{2+} ions. d) Synthesis of droplets via Ca^{2+}-pathway and protocells via Mg^{2+}-pathway. e–l) Information exchange of coacervate droplets and core–shell protocells via different phase separation pathways. e) Strategy and mechanisms of information exchange. f) CLSM images of droplets and protocells. g) Structures swell after washing with 10 mM NaCl TE buffer. h) CLSM images of resulting mixed droplets via Ca^{2+}-pathway. i–j) Line segment analysis of the resulting droplets and Janus-like structure. k) CLSM images of the resulting core–shell protocells with mixed core via Mg^{2+}-pathway. l) Line segment analysis of the obtained protocell. Scale bar: 5 μm. inset: 2 μm.

both $p(A_{20}\text{-}i)_{27}$-based ssDNA from the droplet and the protocell, and the shell localization of $p(T_{20}\text{-}j)_{27}$ is enabled by the absence of phase separation of $p(T_{20}\text{-}j)_{27}$ in the presence of Mg^{2+} ions (Figure 5k,l and Figure S5e). The

formation of various morphologies via performing a temperature ramp on the droplet and protocell mixture achieves pathway-controlled structuration by metal-dependent phase separation of ssDNA polymers, thus offering the possibility of information exchange of DNA biomaterials.

Conclusion

We have systematically investigated the coacervations of ssDNA polymers based on the thermo-responsive phase separation pathways that are important for a fundamental understanding of the phase behavior of nucleic acids in biology and nanoscience, as well as for the formation of DNA droplets and DNA-based protocells as entities to study life-like behavior in complex systems. Significantly, by using a combination of *ex situ* and *in situ* CLSM and DLS, we have identified similarities and distinct differences in the ion-dependent phase separation behavior between Mg^{2+}- and Ca^{2+}-pathways, both of which follow a two-stage process for coacervation of the ssDNA chains. A first critical temperature is found, T_1, whereupon stable nuclei are formed that are much smaller than the optical diffraction limit, followed by a relatively stable temperature region (in terms of turbidity), and eventually, a second transition, T_2, occurs that leads to micron-scale coacervation by growth and coalescence. The T_1 and T_2 regions depend slightly on the overall chain length but more strongly on the counterion concentration. This behavior is robust. The most striking difference between Ca^{2+} and Mg^{2+} as counterions relates to the reversibility of the phase transition. Mg^{2+} has a fully reversible transition, whereas Ca^{2+} clearly leads to irreversible trapping of the coacervate droplets formed at high temperatures. The stronger propensity of Ca^{2+} for coacervate formation also leads to a different selectivity regarding the nucleobases. While Mg^{2+} leads to selective temperature-induced coacervation of polyA-rich ssDNA, whereas polyT-rich ssDNA remains in solution, Ca^{2+} is clearly indiscriminatory and also leads to temperature-induced coacervation of polyT-rich strands. Additionally, we could derive important aspects regarding sphericity and size of the coacervates by showing that an appropriate length is needed to obtain sufficient phase separation, while excessively long strands hinder re-obtaining a spherical shape after droplet coalescence at high temperature.

In summary, these data show that a careful mapping of the system behavior allows delineating distinct differences regarding ion-dependent and temperature-induced phase separation of ssDNA polymers. We put the different strengths of the approaches to work and could show that a Ca^{2+}-derived polyA-rich droplet (that would be unstable in a Mg^{2+} setting) can merge their information content with a Mg^{2+}-derived core/shell DNA protocell formed by a polyA/polyT (that would equally not form in a Ca^{2+}-setting) by proper salinity adjustment and using a secondary temperature ramp.

These phase behavior of sequence-specific nucleic acid polymers may provide an essential understanding of relevant scenarios in living cells, such as heat shock-mediated droplet formation inside the living cell cytoplasm[26] or the relevance of a polyA-tag present in each mRNA produced in the nucleus. Furthermore, our studies also may pave the way toward understanding the "origin of life" scenarios where nucleic acids played an essential role in prebiotic confinements.[10c,27]

Together, these investigations of the phase separation mechanisms offer a better understanding of coacervation of DNA-based systems, properties of membrane-less nucleic acid-rich organelles, and emulating life-like functions in future protocellular systems.

Acknowledgements

We acknowledge support by the DFG within WA 3084/19-1. W. Liu acknowledges the support by the Chinese Scholarship Council (CSC). We thank C. Sharma for helping us with the DLS measurement and M. Sun for the discussion. A.W. acknowledges generous support in the framework of a Gutenberg Research Professorship of the Gutenberg Research College. Open Access funding enabled and organized by Projekt DEAL.

Conflict of Interest

The authors declare no conflict of interest.

Data Availability Statement

The data that support the findings of this study are available from the corresponding author upon reasonable request.

Keywords: Artificial Cell · DNA Nanoscience · Liquid-Liquid Phase Separation · Membrane-Less Organelles · Nucleic Acids

[1] a) S. Alberti, A. Gladfelter, T. Mittag, *Cell* **2019**, *176*, 419–434; b) A. A. Hyman, C. A. Weber, F. Julicher, *Annu. Rev. Cell Dev. Biol.* **2014**, *30*, 39–58; c) Y. Yin, L. Niu, X. Zhu, M. Zhao, Z. Zhang, S. Mann, D. Liang, *Nat. Commun.* **2016**, *7*, 10658; d) S. F. Banani, A. M. Rice, W. B. Peeples, Y. Lin, S. Jain, R. Parker, M. K. Rosen, *Cell* **2016**, *166*, 651–663; e) S. F. Banani, H. O. Lee, A. A. Hyman, M. K. Rosen, *Nat. Rev. Mol. Cell Biol.* **2017**, *18*, 285–298; f) T. Kaur, M. Raju, I. Alshareedah, R. B. Davis, D. A. Potoyan, P. R. Banerjee, *Nat. Commun.* **2021**, *12*, 872.

[2] a) S. K. Goetz, J. Mahamid, *Dev. Cell* **2020**, *55*, 97–107; b) C. P. Brangwynne, P. Tompa, R. V. Pappu, *Nat. Phys.* **2015**, *11*, 899–904.

[3] T. Pederson, *Cold Spring Harbor Perspect. Biol.* **2011**, *3*, a000638.

[4] M. Dundr, M. D. Hebert, T. S. Karpova, D. Stanek, H. Xu, K. B. Shpargel, U. T. Meier, K. M. Neugebauer, A. G. Matera, T. Misteli, *J. Cell Biol.* **2004**, *164*, 831–842.

[5] Y. S. Mao, B. Zhang, D. L. Spector, *Trends Genet.* **2011**, *27*, 295–306.

[6] C. J. Decker, R. Parker, *Cold Spring Harbor Perspect. Biol.* **2012**, *4*, a012286.

[7] a) V. Nandana, J. M. Schrader, *Curr. Opin. Microbiol.* **2021**, *61*, 91–98; b) M. L. Nosella, J. D. Forman-Kay, *Curr. Opin. Cell Biol.* **2021**, *69*, 30–40; c) J. D. O'Connell, A. Zhao, A. D. Ellington, E. M. Marcotte, *Annu. Rev. Cell Dev. Biol.* **2012**, *28*, 89–111.
[8] a) M. Abbas, W. P. Lipinski, J. Wang, E. Spruijt, *Chem. Soc. Rev.* **2021**, *50*, 3690–3705; b) C. A. Strulson, R. C. Molden, C. D. Keating, P. C. Bevilacqua, *Nat. Chem.* **2012**, *4*, 941–946.
[9] N. Martin, *ChemBioChem* **2019**, *20*, 2553–2568.
[10] a) C. Love, J. Steinkuhler, D. T. Gonzales, N. Yandrapalli, T. Robinson, R. Dimova, T. D. Tang, *Angew. Chem. Int. Ed.* **2020**, *59*, 5950–5957; b) K. K. Nakashima, J. F. Baaij, E. Spruijt, *Soft Matter* **2018**, *14*, 361–367; c) A. Samanta, V. Sabatino, T. R. Ward, A. Walther, *Nat. Nanotechnol.* **2020**, *15*, 914–921; d) J. Deng, A. Walther, *Chem* **2020**, *6*, 3329–3343.
[11] R. R. Poudyal, R. M. Guth-Metzler, A. J. Veenis, E. A. Frankel, C. D. Keating, P. C. Bevilacqua, *Nat. Commun.* **2019**, *10*, 490.
[12] a) K. Adamala, J. W. Szostak, *Nat. Chem.* **2013**, *5*, 495–501; b) M. Weiss, J. P. Frohnmayer, L. T. Benk, B. Haller, J. W. Janiesch, T. Heitkamp, M. Borsch, R. B. Lira, R. Dimova, R. Lipowsky, E. Bodenschatz, J. C. Baret, T. Vidakovic-Koch, K. Sundmacher, I. Platzman, J. P. Spatz, *Nat. Mater.* **2018**, *17*, 89–96.
[13] C. G. Palivan, R. Goers, A. Najer, X. Zhang, A. Car, W. Meier, *Chem. Soc. Rev.* **2016**, *45*, 377–411.
[14] S. Yasuhara, S. Yasui, T. Teranishi, K. Chajima, Y. Yoshikawa, Y. Majima, T. Taniyama, M. Itoh, *Nano Lett.* **2019**, *19*, 1688–1694.
[15] M. Ugrinic, A. Zambrano, S. Berger, S. Mann, T. D. Tang, A. deMello, *Chem. Commun.* **2018**, *54*, 287–290.
[16] W. M. J. Aumiller, C. D. Keating, *Nat. Chem.* **2016**, *8*, 129–137.
[17] T. P. Fraccia, T. Z. Jia, *ACS Nano* **2020**, *14*, 15071–15082.
[18] a) Y. Xing, E. Cheng, Y. Yang, P. Chen, T. Zhang, Y. Sun, Z. Yang, D. Liu, *Adv. Mater.* **2011**, *23*, 1117–1121; b) W. Guo, X. J. Qi, R. Orbach, C. H. Lu, L. Freage, I. Mironi-Harpaz, D. Seliktar, H. H. Yang, I. Willner, *Chem. Commun.* **2014**, *50*, 4065–4068; c) J. Li, C. Zheng, S. Cansiz, C. Wu, J. Xu, C. Cui, Y. Liu, W. Hou, Y. Wang, L. Zhang, I. T. Teng, H. H. Yang, W. Tan, *J. Am. Chem. Soc.* **2015**, *137*, 1412–1415.
[19] a) R. Merindol, S. Loescher, A. Samanta, A. Walther, *Nat. Nanotechnol.* **2018**, *13*, 730–738; b) S. Ludwanowski, A. Samanta, S. Loescher, C. Barner-Kowollik, A. Walther, *Adv. Sci.* **2021**, *8*, 2003740.
[20] a) W. Zhao, M. M. Ali, M. A. Brook, Y. Li, *Angew. Chem. Int. Ed.* **2008**, *47*, 6330–6337; b) M. M. Ali, F. Li, Z. Zhang, K. Zhang, D. K. Kang, J. A. Ankrum, X. C. Le, W. Zhao, *Chem. Soc. Rev.* **2014**, *43*, 3324–3341; c) E. J. Cho, L. Yang, M. Levy, A. D. Ellington, *J. Am. Chem. Soc.* **2005**, *127*, 2022–2023; d) M. M. Ali, Y. Li, *Angew. Chem. Int. Ed.* **2009**, *48*, 3512–3515; *Angew. Chem.* **2009**, *121*, 3564–3567.
[21] a) C. Ralec, E. Henry, M. Lemor, T. Killelea, G. Henneke, *Nucleic Acids Res.* **2017**, *45*, 12425–12440; b) N. Korolev, A. P. Lyubartsev, A. Rupprecht, L. Nordenskiöld, *Biophys. J.* **1999**, *77*, 2736–2749; c) S. R. Bellamy, Y. S. Kovacheva, I. H. Zulkipli, S. E. Halford, *Nucleic Acids Res.* **2009**, *37*, 5443–5453.
[22] R. Ahmad, H. Arakawa, H. A. Tajmir-Riahi, *Biophys. J.* **2003**, *84*, 2460–2466.
[23] H.-T. Xu, N. Zhang, M.-R. Li, F.-S. Zhang, *J. Mol. Liq.* **2021**, *344*, 117781.
[24] a) E. V. Hackl, S. V. Kornilova, Y. P. Blagoi, *Int. J. Biol. Macromol.* **2005**, *35*, 175–191; b) M. Langlais, H. A. Tajmir-Riahi, R. Savoie, *Biopolymers* **1990**, *30*, 743–752.
[25] Y.-H. Wu, D.-M. Wang, J.-Y. Lai, *J. Phys. Chem. B* **2008**, *112*, 4604–4612.
[26] a) B. Wang, B. A. Maxwell, J. H. Joo, Y. Gwon, J. Messing, A. Mishra, T. I. Shaw, A. L. Ward, H. Quan, S. M. Sakurada, S. M. Pruett-Miller, T. Bertorini, P. Vogel, H. J. Kim, J. Peng, J. P. Taylor, M. Kundu, *Mol. Cell Mol. Cell.* **2019**, *74*, 742–757; b) Y. Gwon, B. A. Maxwell, R.-M. Kolaitis, P. Zhang, H. J. Kim, J. P. Taylor, *Science* **2021**, *372*, eabf6548.
[27] A. Samanta, M. Horner, W. Liu, W. Weber, A. Walther, *Nat. Commun.* **2022**, *13*, 3968.

Manuscript received: June 20, 2022
Accepted manuscript online: September 16, 2022
Version of record online: October 7, 2022